Journal of Environmental Chemical Engineering 13 (2025) 119273

Contents lists available at ScienceDirect

Journal of Environmental Chemical Engineering

journal homepage: www.elsevier.com/locate/joce

Graphite decorated Pt/α-Fe_2O_3 composite with outstanding CO oxidation performance in the presence of SO_2 and moisture

Xinru Qi, Xiaoxuan Fan, Liang Li *

Key Laboratory for Ultrafine Materials of Ministry of Education, School of Materials Science and Engineering, East China University of Science and Technology, Shanghai 200237, China

ARTICLE INFO

Keywords:
CO oxidation
Catalyst
Sulfur resistance
Pt

ABSTRACT

A graphite-decorated Pt/α-Fe_2O_3 composite with ultra-low Pt content was successfully developed via co-precipitation and surface engineering. The integration of hydrophobic expanded graphite (EG) with the redox-active Pt/α-Fe_2O_3 significantly enhances CO catalytic oxidation activity and resistance to poisoning. Complete CO conversion was achieved below 100 °C at a space velocity of 30,000 $mL \cdot g^{-1} \cdot h^{-1}$, significantly outperforming conventional Pt/α-Fe_2O_3 (150 °C) and reported catalysts, such as Pt/CeO_2 (120 °C) and Pt/ZrO_2 (135 °C). X-ray photoelectron spectroscopy (XPS) revealed no sulfur accumulation on the catalyst's surface after a 48-hour durability test in simulated steel flue gas, indicating excellent SO_2 and moisture tolerance. These features highlight its promise for fuel gas purification and automotive exhaust treatment in sulfur-rich environments.

1. Introduction

The iron and steel industry, as a cornerstone of modern infrastructure and a major energy consumer, emits vast quantities of flue gas containing multiple hazardous components during high-temperature operations [1,2]. Although significant efforts have been made to reduce sulfur dioxide (SO_2) and nitrogen oxides (NO_x) emissions, the residual flue gas remains chemically complex, typically containing high concentrations of carbon monoxide (CO, ~5000 mg/Nm^3), 35–50 ppm SO_2, and 10–15 % water vapor [3]. This harsh and corrosive environment imposes substantial challenges on conventional CO oxidation catalysts. Among these challenges, sulfur and moisture poisoning are the most critical. SO_2 is readily oxidized on catalyst surfaces to form thermodynamically stable sulfate species, which irreversibly block active sites and impair catalytic performance. Concurrently, water vapor competes with CO for surface adsorption and promotes SO_2 oxidation, further accelerating sulfate deposition [4–6]. This synergistic deactivation effect often results in the rapid loss of catalytic activity, typically within tens of hours under real-world flue gas conditions.

To address this issue, recent advances in CO oxidation catalysis have increasingly emphasized strategies to mitigate SO_2 poisoning and moisture-induced deactivation. Approaches based on material design, such as rare-earth doping of CeO_2 [7] or the development of Mn–Co spinels [8], have been shown to enhance lattice oxygen mobility and sulfate tolerance. At the surface level, modifications including Pd encapsulation within TiO_2 or Sn incorporation into Pt/TiO_2 can effectively shield active sites and fine-tune electronic properties, thereby improving resistance to sulfur attack [9]. Structural engineering has also emerged as a powerful tool, exemplified by the confinement of Pt clusters within hydrophobic zeolites to limit H_2O adsorption [10], the application of ultrathin Fe_2O_3 overlayers to regulate sulfate deposition, and the integration of sacrificial SO_2-trapping sites or hydrophobic surface coatings to further prolong catalyst lifetime. In parallel, growing attention has been directed to support engineering and metal alloying, which provide more versatile control over both the structural and electronic environment of catalysts. Strong metal–support interactions not only stabilize and disperse active sites but also inhibit aggregation and deactivation, while alloying strategies can tune the electronic structure of the active phase, optimize adsorption energetics of reaction intermediates, and enhance durability under harsh operating conditions. Compared with conventional compositional or surface modifications, these approaches offer a more robust means of balancing activity with stability. Despite these advances, fundamental challenges remain, particularly in reconciling high catalytic activity with long-term resistance to sulfur and water, elucidating the pathways of sulfate-induced deactivation, and ensuring adequate thermal stability for practical high-temperature applications.

Recently, our group developed a hydrophobic Pt/CeO_2 catalyst

* Corresponding author.
E-mail address: lliliang@ecust.edu.cn (L. Li).

https://doi.org/10.1016/j.jece.2025.119273
Received 22 July 2025; Received in revised form 24 August 2025; Accepted 12 September 2025
Available online 13 September 2025

modified with silane coupling agents, achieving 100 % CO conversion and excellent stability in the presence of SO_2 and water vapor [11]. However, the practical application of this system is hindered by the thermal instability of organic modifiers, which limits its usability under elevated temperatures commonly encountered in steel plant environments. To overcome this limitation, we propose a novel surface modification strategy using inorganic graphite as a thermally stable and chemically inert hydrophobic material. Unlike organic silanes, graphite not only imparts hydrophobicity and suppresses water-induced deactivation but also maintains its structural integrity at high temperatures. By mechanically integrating graphite with Pt/α-Fe_2O_3 with ultra-low noble metal loading content [12], we construct a robust composite catalyst that simultaneously achieves high CO oxidation activity and resistance to both sulfur and moisture poisoning. This design presents a practical and scalable approach for long-term CO elimination in steel flue gas treatment systems. Specifically, the goal of this work is to design and investigate a Pt/α-Fe_2O_3-EG composite catalyst with enhanced SO_2/H_2O resistance for CO oxidation and to demonstrate its long-term stability under harsh reaction conditions.

2. Materials and methods

2.1. Materials and reagents

All the reagents are purchased from Alading Chem. Co. Company and directly used without any purification.

2.2. Materials preparation

Pt/α-Fe_2O_3 composites were synthesized via co-precipitation using NaOH as the precipitation agent. Briefly, 8.34 g $FeSO_4{\cdot}7\ H_2O$ was dissolved in 100 mL deionized water and stirred at 80 °C for 30 min. Then, 2 mL of 0.01 mol·L^{-1} sodium citrate and varying amounts of 0.1 mol·L^{-1} $H_2PtCl_6{\cdot}6\ H_2O$ were added, followed by 50 mL of 2 mol·L^{-1} NaOH. After a 2 h reaction, the precipitate was washed, centrifuged, and dried at 60 °C to yield Pt/Fe_3O_4, which was calcined at 200 °C for 8 h to obtain Pt/α-Fe_2O_3. Samples with 0.05–0.20 wt% Pt were prepared. Pure α-Fe_2O_3 was synthesized similarly without the addition of $H_2PtCl_6{\cdot}6\ H_2O$.

2.3. Graphite modification

Pt/α-Fe_2O_3 composites were mixed and ground with a certain amount of expanded graphite (EG) to achieve Pt/α-Fe_2O_3-EG composites, with an EG mass fraction of 10 wt%.

2.4. Material characterizations

ICP-OES (Agilent 725) was used for elemental analysis. XRD patterns were obtained on a Bruker D8 Focus diffractometer with Cu Kα radiation (λ = 0.15405 nm). N_2 adsorption-desorption isotherms were measured on a TriStar II 3020 analyzer; surface areas and pore distributions were calculated by the BET and BJH methods, respectively. TEM and EDS mapping were performed on an FEI TALOS F200X microscope (200 kV). XPS analysis was conducted using a Thermo Fisher K-Alpha spectrometer (Al Kα, 1486.6 eV) with energy calibration referenced to C 1 s at 284.8 eV. H_2-TPR and CO- TPD were carried out on a ChemBET Pulsar system with TCD detection.

2.5. CO oxidation properties

CO oxidation tests were carried out in a fixed-bed quartz reactor loaded with 0.10 g of catalyst. The feed gas consisted of 1.0 vol% CO, 15.0 vol% O_2, 10.0 vol% H_2O, 100 ppm SO_2, and balance N_2, with a total flow rate of 50 mL·min^{-1} regulated by mass flow controllers, corresponding to a WHSV of 30,000 mL·g^{-1}·h^{-1}. The temperature was ramped from 25 to 250 °C at 5 °C·min^{-1}. Once the CO conversion stabilized at 250 °C, the reactor was cooled stepwise, and data were recorded at each temperature point. For sulfur tolerance evaluation, the catalyst was exposed to the SO_2-containing stream for 48 h under isothermal conditions, with conversion monitored every 4 h. CO concentrations were quantified using a GC-2060 gas chromatograph equipped with a methanizer and FID.

The CO conversion was calculated using the following equation:

$$CO_{conversion}\ (\%) = (S_{CO}^{in} - S_{CO}^{out}) / S_{CO}^{in} * 100$$

where S_{CO}^{in} and S_{CO}^{out} represent the initial CO peak area detected by GC before and after the catalytic reaction, respectively.

All catalytic activity tests and characterizations were repeated at least two times to confirm reproducibility. The results showed negligible variation between runs, and the representative data presented in the figures are consistent with those obtained in repeated experiments.

3. Results and discussion

Scheme 1 illustrates the construction and application strategy of the Pt/α-Fe_2O_3-EG composite. The material was synthesized via a co-precipitation method combined with a surface graphite modification. Pt loadings (0.05, 0.10, 0.15, and 0.20 wt%) were determined by inductively coupled plasma optical emission spectrometry (ICP-OES, Agilent 725, Thermo Scientific), with deviations within ±5 % of the theoretical values, confirming the precise control over noble metal content.

3.1. Structural characterization

The crystalline structure of graphite decorated Pt/α-Fe_2O_3 composite (Pt/α-Fe_2O_3-EG) with varying noble metal loadings was initially characterized by X-ray diffraction (XRD), as shown in Fig. 1. All samples exhibited a series of symmetric Bragg diffraction peaks at approximately 30.3°, 35.6°, 43.3°, 53.8°, 54.9°, 57.5°, 62.6°, 71.5°, and 74.5°, which can be indexed to the (206), (119), (0012), (2212), (500), (1115), (4012), (2018), and (3315) crystallographic planes of hematite-structured Fe_2O_3 (PDF No. 25–1402). The characteristic peaks observed at 2θ = 35.6°, 43.3°, 57.5°, and 62.6° were attributed to the presence of α-Fe_2O_3 phase in the iron oxide support material [13]. The diffraction peak at 2θ = 26.4° corresponds to the (002) plane of expanded graphite (EG), consistent with the reference pattern (PDF No. 41–1487) [14]. The XRD patterns of Pt/α-Fe_2O_3-EG closely resemble those of the Fe_2O_3 support. According to ICP-OES analysis, the actual Pt loadings were 0.05 wt%, 0.10 wt%, 0.15 wt%, and 0.20 wt%, respectively. No discernible diffraction peaks corresponding to metallic Pt were detected, likely due to the low Pt content, which was insufficient to produce detectable singles. This also indicates that the Pt nanoparticles

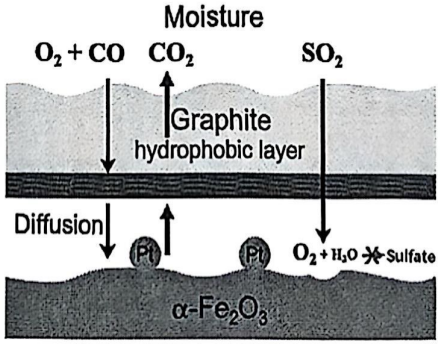

Scheme 1. Schematic illustration for the construction of Pt/α-Fe_2O_3-EG composite and its application for CO oxidation in the presence of H_2O and SO_2.

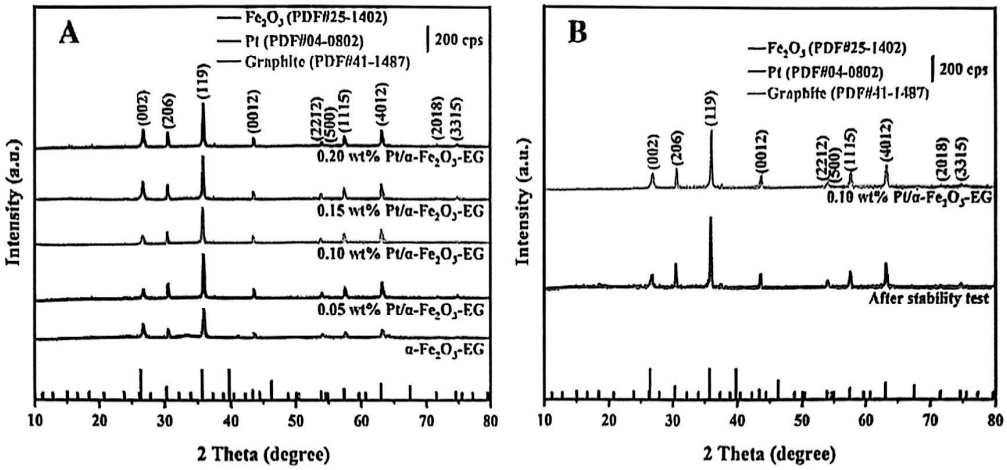

Fig. 1. (A) XRD patterns of the Pt/α-Fe_2O_3-EG nanocomposites with different Pt contents, and (B) before and after the 0.10 wt% Pt/α-Fe_2O_3-EG CO oxidation durability test.

in the Pt/α-Fe_2O_3 catalyst are extremely small and highly dispersed on the support surface [15]. Furthermore, after the 48-hour catalytic stability test for CO oxidation in the presence of SO_2 and H_2O, no detectable sulfate phases were observed in the diffraction pattern (Fig. 1B). Such "clean" surface characteristics facilitate the exposure of more active sites, thereby providing a stable catalyst for enhanced CO catalytic oxidation activity.

The microstructure and morphology of the Pt/α-Fe_2O_3-EG composite were thoroughly characterized using transmission electron microscopy (TEM). As shown in Fig. 2A, a representative TEM image of the 0.10 wt%

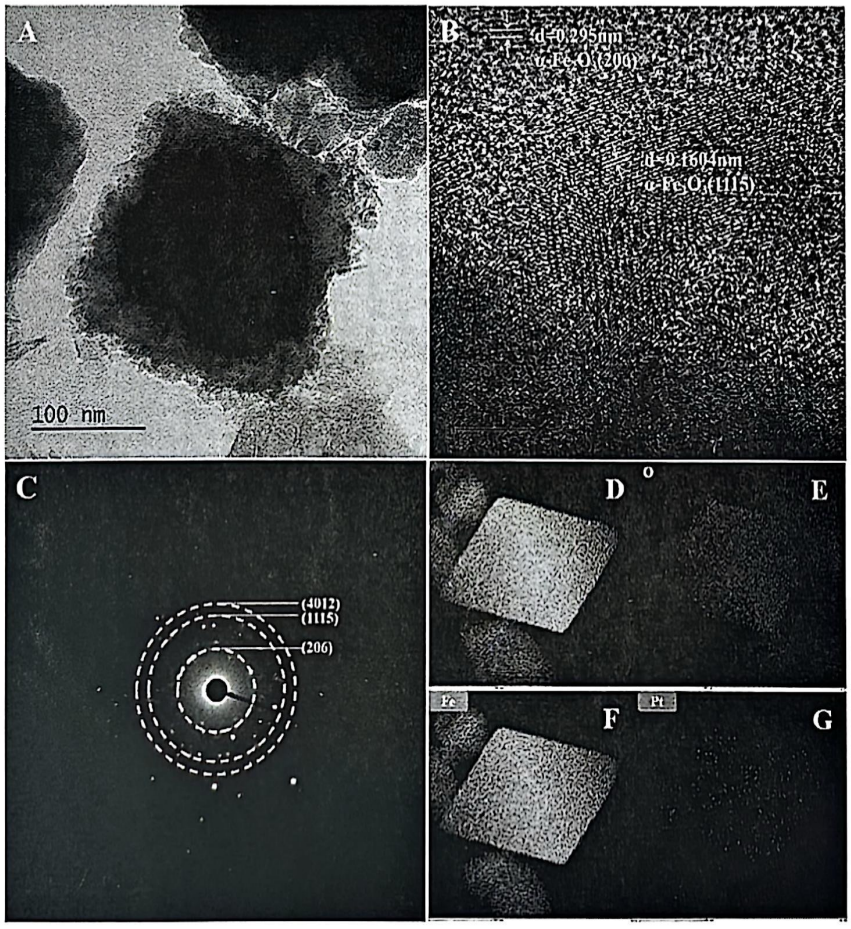

Fig. 2. TEM image (A); HRTEM image (B) and corresponding selected area electron diffraction (SAED) pattern(C); HAADF-STEM (D) and corresponding O, Fe, and Pt elemental mapping images (E-G) of the 0.10 wt% Pt/α-Fe_2O_3-EG composite.

Pt/α-Fe_2O_3-EG sample displays well-defined nanocubic structures of the α-Fe_2O_3 support. High-resolution TEM (HRTEM) analysis (Fig. 2B) reveals distinct lattice spacings of 0.295 nm and 0.1604 nm, corresponding to the (206) and (1115) planes of α-Fe_2O_3 (JCPDS 25–1402), respectively, which is consistent with the XRD results. Notably, no lattice fringes characteristic of metallic Pt, such as the 0.226 nm spacing of the Pt(111) plane, were observed in the HRTEM images[16]. This absence is primarily attributed to the extremely low Pt loading (0.10 wt %), which renders its lattice signal below the detection limit of the instrument. Moreover, the Pt species are likely present as highly dispersed ultrafine nanoparticles on the support surface, preventing the formation of larger crystalline domains.

Selected-area electron diffraction (SAED) pattern analysis (Fig. 2C) further elucidates the crystalline features of the material. The presence of continuous and well-defined diffraction rings corresponding to the (206), (1115), and (4012) planes of α-Fe_2O_3 is in excellent agreement with the XRD results, confirming the high crystallinity of the support. The absence of diffraction signals attributable to metallic platinum can be ascribed not only to the ultralow Pt loading but also to the possibility that the supported Pt nanoparticles are either amorphous or possess defect-rich surface structures. Energy-dispersive X-ray spectroscopy (EDS) elemental mapping (Fig. 2D–G) reveals a uniform distribution of Fe and O elements throughout the material [17]. Although the Pt signal is relatively weak, it nonetheless indicates a well-dispersed distribution, with no apparent aggregation or clustering observed.

Fig. 3 presents the N_2 adsorption–desorption isotherms and corresponding pore size distributions of Pt/α-Fe_2O_3-EG composites with varying noble metal loadings. All isotherms exhibit typical Type IV characteristics with H_3-type hysteresis loops, consistent with the IUPAC classification, indicating the presence of slit-shaped mesopores and macropores [18]. The negligible adsorption at low relative pressures ($P/P_0 < 0.3$) suggests a lack of micropores and limited accessible mesoporosity. The notable increase in adsorption capacity at higher relative pressures ($P/P_0 > 0.5$) can be attributed to multilayer adsorption and capillary condensation within the macroporous network. This porous architecture is derived primarily from interparticle voids between catalyst particles and the interlayer structure of expanded graphite (EG). The BET surface area remains relatively low and shows minimal variation with increasing Pt content [19], consistent with the macroporous nature of the composite. Pore size distribution profiles further confirm a broad pore size range extending well into the macropore region. Although nitrogen physisorption is less sensitive to pores larger than 50 nm, the results indicate a uniform and hierarchical pore structure that is beneficial for mass transport and catalytic performance. Importantly, the pore size distribution and pore volume remain largely unchanged with Pt loading, demonstrating that the incorporation of noble metal has negligible impact on the overall structural properties of the composite.

XPS was employed to investigate the surface chemical states of the Pt/α-Fe_2O_3-EG catalyst before and after the stability test under 100 ppm SO_2 and 10 % H_2O, as shown in Fig. 4. The O 1 s spectrum (Fig. 4A) displays two peaks at −530.25 eV and −532.09 eV, corresponding to lattice oxygen and chemisorbed oxygen in α-Fe_2O_3, respectively[20,21]. The S 2p spectrum (Fig. 4B) of the fresh catalyst exhibits doublets at

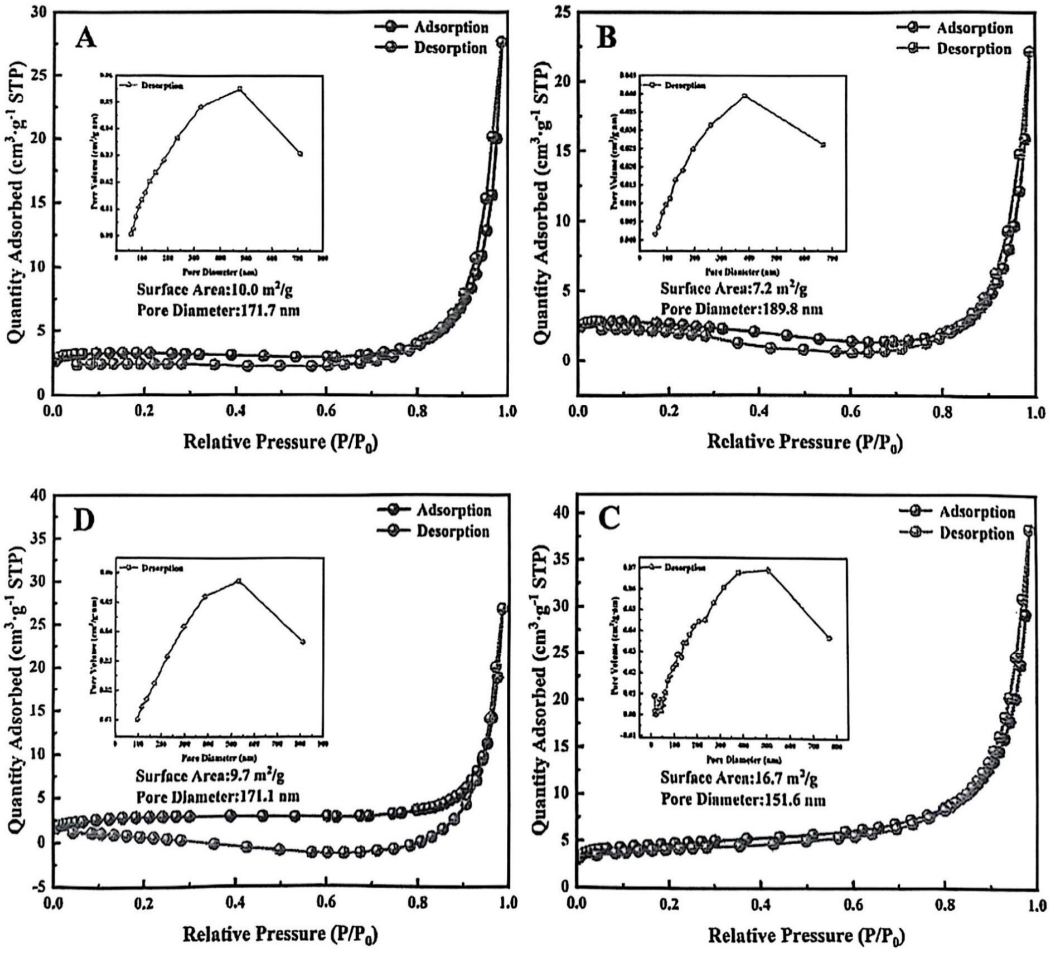

Fig. 3. The N_2 adsorption-desorption isotherms of Pt/α-Fe_2O_3-EG (A) 0.05 wt% Pt, (B) 0.10 wt% Pt, (C) 0.15 wt% Pt, and (D) 0.20 wt% Pt.

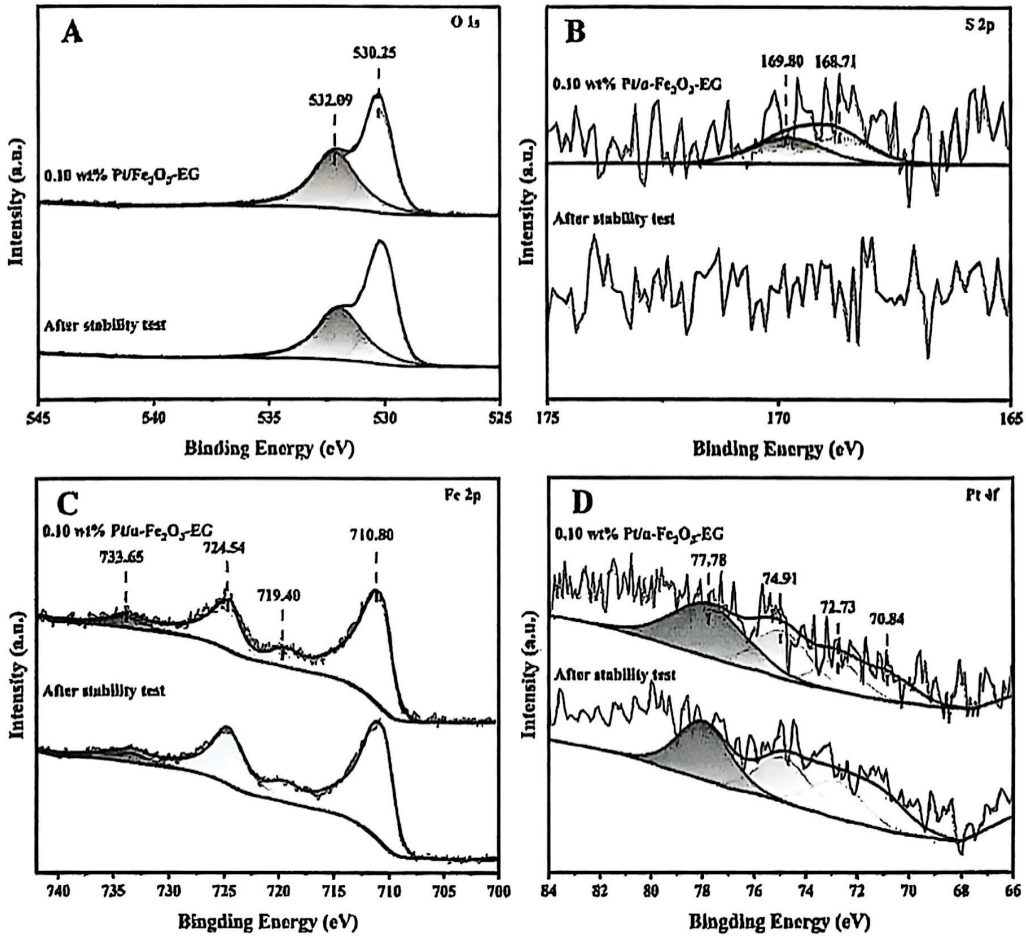

Fig. 4. XPS spectra of 0.10 wt% Pt/α-Fe_2O_3-EG, hydrophobic 0.10 wt% Pt/α-Fe_2O_3-EG before and after the CO oxidation durability test. O 1 s (A), S 2p (B), Fe 2p (C), and Pt 4 f (D).

168.71 eV and 169.80 eV, assigned to residual sulfate species originating from the $FeSO_4$·7 H_2O precursor[22]. After 48 h of testing, these peaks nearly disappear, indicating the removal or transformation of surface sulfates, likely due to surface reconstruction and sulfur volatilization. This confirms the strong sulfur resistance of the composite.

The Fe 2p spectrum (Fig. 4C) exhibits characteristic peaks at binding energies of 710.80 eV (Fe $2p_{3/2}$) and 724.54 eV (Fe $2p_{1/2}$), accompanied by satellite features at 719.40 eV and 733.65 eV. Deconvolution analysis confirms that the spectral components correspond exclusively to Fe^{3+} species [23,24], with no detectable Fe^{2+} signatures. The characteristic binding energies and spectral line shape are indicative of the α-Fe_2O_3 phase. Quantitative analysis reveals 100 % Fe^{3+} occupancy, confirming phase purity. Critically, the Fe 2p profile remains unchanged after stability testing, demonstrating the structural integrity of α-Fe_2O_3 under reaction conditions. This complete Fe^{3+} retention is attributed to Pt-mediated electron transfer, which stabilizes the oxidation state and inhibits reduction. Pt incorporation may help maintain the Fe^{3+} state via electron transfer, enhancing lattice oxygen activity for CO oxidation through the Mars–van Krevelen mechanism. The Pt 4 f spectrum (Fig. 4D) shows signals for both Pt^0 (70.84 and 74.91 eV) and Pt^{2+} (72.73 and 77.78 eV) [25], implying partial oxidation of Pt due to interfacial Pt–O–Fe interactions. This electron transfer from Pt to α-Fe_2O_3 may facilitate oxygen vacancy formation. Notably, no significant changes in Fe and Pt states are observed after testing, demonstrating the excellent structural stability and anti-poisoning ability of the catalyst.

The reduction behavior of the synthesized catalysts was investigated by H_2 temperature-programmed reduction (H_2-TPR), and the results are

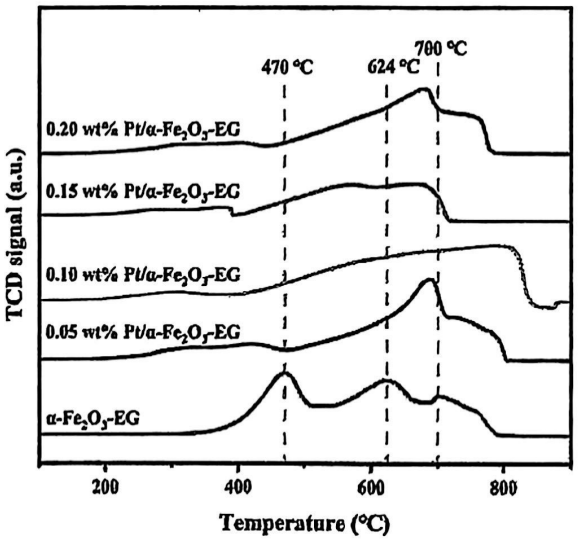

Fig. 5. H_2-TPR curves of the pure α-Fe_2O_3-EG and Pt/α-Fe_2O_3-EG composites.

shown in Fig. 5. The pristine α-Fe_2O_3-EG sample exhibited three distinct reduction peaks. The first peak, appearing at approximately 470 °C, is assigned to the reduction of α-Fe_2O_3 to Fe_3O_4 [26]. A broad reduction feature between 600 and 800 °C consists of two overlapping peaks centered at −624 °C and −700 °C, which correspond to the stepwise reductions of Fe_3O_4 to FeO and FeO to metallic Fe, respectively [27]. Upon the incorporation of Pt, the Pt/α-Fe_2O_3-EG catalyst showed a significant shift in the reduction profile, characterized by a decreased initial reduction temperature and reduced peak area. These changes suggest enhanced reducibility, likely due to the ability of Pt to dissociate H_2 and promote hydrogen spillover, thereby weakening the Fe–O bonds. In addition, the presence of Pt may improve the dispersion of α-Fe_2O_3 or alter the local electronic environment of Fe species through the formation of Pt–Fe interfacial structures. These effects can facilitate the selective reduction of Fe^{3+} to Fe^{2+}, favoring the formation of Fe_3O_4 while suppressing further reduction to lower-valence iron species [28], which may contribute to the observed decrease in overall hydrogen consumption. Notably, no reduction peaks related to PtO_x species were observed in any of the Pt-containing samples, possibly due to the low Pt loading or the reduction events occurring outside the temperature range investigated [29]. Within the detection limits of the instrument, this suggests that Pt is predominantly present in the metallic state during TPR analysis. In summary, the introduction of Pt enhances the reducibility of α-Fe_2O_3 and promotes its selective transformation to Fe_3O_4, providing mechanistic insights into the construction of active sites and the design of more efficient catalytic systems.

To investigate the CO adsorption properties of the catalysts, CO-TPD analysis was conducted, and the results are shown in Fig. 6. Both the Pt/α-Fe_2O_3-EG catalysts with varying Pt loadings (0.05–0.20 wt%) and the pristine α-Fe_2O_3-EG support exhibited CO desorption peaks at around 880 °C and 1000–1050 °C, indicating the presence of strongly chemisorbed CO species on the surface [30]. This strong adsorption behavior is attributed to the synergistic effect between Pt-Fe_2O_3 interfacial interactions and oxygen vacancies in the support. The CO desorption peak of α-Fe_2O_3-EG at ~880 °C appeared at a higher temperature compared to that of Pt/α-Fe_2O_3-EG. As the Pt loading increased, the desorption peak shifted to lower temperatures, suggesting a decrease in CO binding energy and an increase in the number and activity of adsorption sites. The 0.15 wt% Pt/α-Fe_2O_3-EG catalyst exhibited a shoulder peak in the desorption profile at ~1000 °C [31], which may originate from the formation of abundant Pt-Fe_2O_3 interfacial sites at higher Pt loadings, along with enhanced metal-support electronic interactions or spillover effects, thereby strengthening the chemical bonding between CO molecules and the catalyst surface [32]. The introduction of Pt significantly modulates the electronic structure of the support, leading to a notable improvement in CO adsorption capacity. The 0.20 wt% Pt/α-Fe_2O_3-EG catalyst demonstrated superior CO adsorption performance, which correlates well with its enhanced catalytic activity. This improvement can be ascribed to the stronger CO adsorption facilitates the stabilization of reaction intermediates, ultimately improving catalytic activity and selectivity.

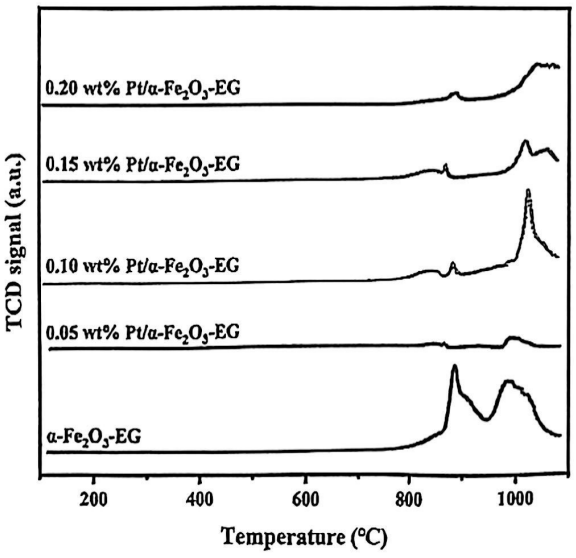

Fig. 6. CO-TPD curves of the pure α-Fe_2O_3-EG and Pt/α-Fe_2O_3-EG composites.

3.2. Catalytic properties and SO_2 resistance

As shown in Fig. 7A, the CO oxidation performance of the graphite-decorated Pt/α-Fe_2O_3-EG composites was evaluated under the coexistence of SO_2 and H_2O. As the Pt loading increased from 0.05 wt% to 0.20 wt%, the temperature required for complete CO conversion steadily decreased from 140 °C to 90 °C, with the 0.20 wt% sample exhibiting the highest catalytic activity. The introduction of hydrophobic expanded graphite (EG) significantly enhanced the CO oxidation performance of the Pt/α-Fe_2O_3 catalyst. Compared to the unmodified 0.10 wt% Pt/α-Fe_2O_3 catalyst (complete CO conversion at 180 °C), the EG-modified 0.10 wt% Pt/α-Fe_2O_3-EG exhibited a lower complete conversion temperature and superior poisoning resistance. These experimental results clearly demonstrate that EG incorporation effectively improves the catalytic performance of the Pt/α-Fe_2O_3 system. Particularly noteworthy is that the Pt-free α-Fe_2O_3-EG support showed only 61.9 % CO conversion at 250 °C and complete deactivation at 140 °C, which provides compelling evidence for the pivotal role of Pt active sites in the catalytic reaction. The Pt nanoparticles act as the primary active centers, significantly lowering the reaction's activation energy by promoting CO adsorption/activation and O_2 dissociation. Furthermore, strong metal–support interactions (SMSI) at the Pt/α-Fe_2O_3 interface induce synergistic effects that modulate the electronic structure, thereby facilitating oxygen vacancy regeneration and enhancing lattice oxygen mobility, likely following the Mars–van Krevelen mechanism. The catalytic performance is dependent on Pt loading: as the Pt content increases from 0.05 wt% to 0.20 wt%, the surface density of active sites increases while maintaining high Pt dispersion, resulting in a substantial improvement in intrinsic catalytic activity [33].

Due to the low Pt loading (0.05–0.20 wt%), surface Pt atomic fractions from XPS were used to estimate active sites for TOF calculations, allowing reliable comparison of intrinsic activity trends. The TOF for 0.10 wt% Pt/α-Fe_2O_3-EG composite is estimated of 2.6 s^{-1} at 120 °C. Incorporation of expanded graphite (EG) enhances structural stability and provides local hydrophobic protection; although the catalyst is not fully covered (SEM image in supporting information) and contact angle measurements are not feasible, TEM/XPS analyses and stable CO conversion under 100 ppm SO_2 and 10 % H_2O support this effect. H_2-TPR profiles qualitatively reveal the $Fe^{3+} \rightarrow Fe^{2+} \rightarrow Fe^0$ reduction sequence, indicating enhanced reducibility and strong metal–support interactions. Overall, uniform Pt dispersion, EG-mediated protection, and metal–support interactions underpin high activity and stability.

Considering typical steel mill flue gas conditions—often above 100 °C—and catalyst cost, a Pt loading of 0.10 wt% was chosen for the stability test. As shown in Fig. 7B, the 0.10 wt% Pt/α-Fe_2O_3-EG catalyst maintained 100 % CO conversion over 48 h at 200 °C with a space velocity of 30,000 $mL \cdot g^{-1} \cdot h^{-1}$. The outstanding stability is mainly due to expanded graphite (EG), whose hydrophobic surface suppresses water adsorption and sulfate deposition, preserving active sites as confirmed by XPS. Further enhancing EG's structure or interfacial properties could improve catalyst dispersion and mass transfer, thus boosting activity and poisoning resistance [34,35].

The structural characterization and surface analyses provide a clear explanation for the observed catalytic performance. XRD patterns confirmed the formation of α-Fe_2O_3 and the presence of highly dispersed Pt nanoparticles, which was further supported by TEM images showing

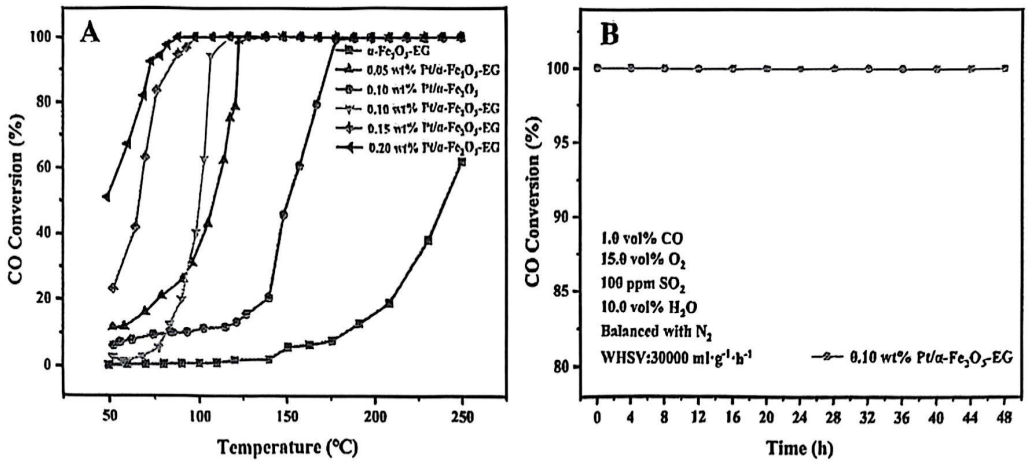

Fig. 7. CO catalytic oxidation properties (A); CO oxidation stability test for the 0.10 wt% Pt/α-Fe_2O_3-EG nanocomposite at 200 °C (B). (Reaction conditions: 1.0 vol % CO, 15.0 vol% O_2, 100 ppm SO_2, 10.0 vol% H_2O balanced with N_2, catalystamount: 100 mg, WHSV:30000 mL·g^{-1}·h^{-1}).

uniform Pt distribution on the expanded graphite-supported α-Fe_2O_3. XPS analysis revealed that the Pt species maintained a favorable oxidation state and strong interaction with the support, contributing to the stability of active sites. These structural and electronic features correlate directly with the catalytic results: the Pt/α-Fe_2O_3-EG composite exhibited superior CO conversion, even under harsh conditions containing SO_2 and H_2O. Furthermore, the hydrophobicity of EG within the composite, helped suppress deactivation by moisture, explaining the catalyst's excellent long-term stability. Collectively, these findings demonstrate that the synergistic combination of optimized structure, surface properties, and electronic interactions is key to achieving high activity and durability in CO oxidation.

3.3. Reaction kinetics of catalysts

To assess the efficiency of the hydrophobically modified catalysts, the apparent activation energy (Ea) for CO oxidation over Pt/α-Fe_2O_3-EG composites was determined via Arrhenius plots (Fig. 8). Keeping CO conversion below 15 %, the rate constant (k) increased and Ea decreased with higher Pt loadings (0–0.20 wt%). Ea values for α-Fe_2O_3-EG and 0.05, 0.10, 0.15, 0.20 wt% Pt composites were 79.4, 74.7, 57.2, 40.3, and 24.4 kJ·mol^{-1}, respectively. The 0.20 wt% Pt catalyst showed the lowest Ea, correlating with its highest activity and improved reducibility from H_2-TPR results [36,37].

While in situ spectroscopic studies and kinetic modeling were not performed in this work, the observed trends in CO oxidation activity, combined with structural and surface characterization, provide strong evidence for the roles of Pt dispersion, metal–support interactions, and EG hydrophobicity. Future studies will include DRIFTS and kinetic modeling to further investigate reaction mechanisms and identify active sites.

4. Conclusion

A novel hydrophobic Pt/α-Fe_2O_3-EG catalyst with ultra-low Pt loading (<0.20 wt%) was developed, exhibiting excellent CO oxidation performance and strong sulfur resistance below 100 °C in simulated steel mill flue gas. The expanded graphite enhances hydrophobicity and suppresses H_2O adsorption, while the α-Fe_2O_3–Pt interaction promotes oxygen activation and mitigates sulfate deposition. The catalyst maintained full CO conversion over 48 h at 200 °C, demonstrating outstanding durability under harsh conditions. These results provide valuable insights into the design of durable catalysts for sulfur-containing flue gas treatment. Future research could focus on optimizing catalyst composition and structure for large-scale industrial applications, as well as exploring the applicability to other flue gas pollutants.

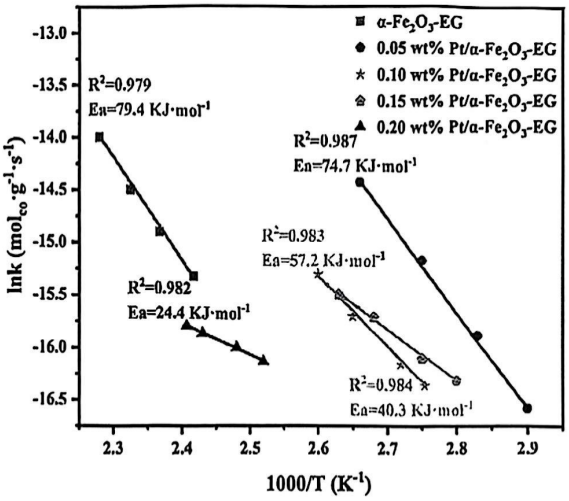

Fig. 8. Arrhenius plots of CO oxidation reaction rate (activation energy, Ea) over hydrophobic Pt/α-Fe_2O_3-EG composites with different Pt loading contents.

CRediT authorship contribution statement

Li Liang: Writing – review & editing, Supervision. **Xinru Qi:** Writing – original draft, Formal analysis. **Xiaoxuan Fan:** Data curation.

Declaration of Competing Interest

The authors declare that they have no known competing financial interests or personal relationships that could have appeared to influence the work reported in this paper.

Acknowledgements

None.

Appendix A. Supporting information

Supplementary data associated with this article can be found in the

online version at doi:10.1016/j.jece.2025.119273.

Data availability

Data will be made available on request.

References

[1] Z. Shen, X. Xing, Y. She, S. Wang, M. Lv, J. Li, H. Li, Revealing of K and SO_2 poisoning mechanism on $CuCeO_x$ catalyst for low-temperature CO oxidation, Chem. Eng. J. 485 (2024) 149373.

[2] L. Ni, X. Gao, L. Qian, L. Ding, H. Long, Poisoning mechanism of potassium salts on catalytic oxidation of CO over $CeMnO_2$ catalysts in sintering flue gas, J. Environ. Chem. Eng. 13 (2025) 117612.

[3] Z. Xu, Y. Li, Y. Lin, Y. Wang, Q. Wang, T. Zhu, Loading mechanism and double-site reaction mechanism of Cu on activated carbon for enhanced oxidation of CO from flue gas, Chem. Eng. J. 419 (2021) 129994.

[4] X. Liu, Y. Zou, X. Li, T. Xu, W. Cen, B. Li, T. Zhu, Ultralow doping of mn species into Pt catalyst enhances the CO oxidation performance in the presence of H_2O and SO_2, ACS Catal. 13 (2023) 14580–14597.

[5] J. Chen, Y. Su, Q. Meng, H. Qian, L. Shi, J.A. Darr, Z. Wu, X. Weng, Palladium encapsulated by an Oxygen-Saturated TiO_2 overlayer for Low-Temperature SO_2-Tolerant catalysis during CO oxidation, Angew. Chem. Int. Ed. 62 (2023) e202310191.

[6] Y. Liu, C. Ma, J. Wang, W. Qiao, L. Ling, Low-content doped CoMOx (M = Co, Fe, Ni, Cu) spinel derived from kolwezite-like carbonate hydroxide for low-temperature CO oxidation with enhanced water and sulfur resistance, J. Environ. Chem. Eng. 13 (2025) 116588.

[7] Y. Deng, P. Tian, S. Liu, H. He, Y. Wang, L. Ouyang, S. Yuan, Enhanced catalytic performance of atomically dispersed Pd on Pr-doped CeO_2 nanorod in CO oxidation, J. Hazard. Mater. 426 (2022) 127793.

[8] F. Gao, C. Chu, W. Zhu, X. Tang, H. Yi, R. Zhang, High-efficiency catalytic oxidation of nitric oxide over spherical Mn Co spinel catalyst at low temperature, Appl. Surf. Sci. 479 (2019) 548–556.

[9] I. Borbáth, K. Salmanzade, Z. Pászti, A. Kuncser, D. Radu, Ş. Neaţu, E. Tálas, I. E. Sajó, D. Olasz, G. Sáfrán, Á. Szegedi, M. Florea, A. Tompos, Strategies to improve CO tolerance and corrosion resistance of Pt electrocatalysts for polymer electrolyte membrane fuel cells: Sn-doping of the mixed oxide–carbon composite support, Catal. Today 438 (2024) 114788.

[10] Y. Li, P. Liang, Y. Yu, X. Min, G. Wang, B. Zhao, T. Sun, Unravelling the enhanced water-promotion effect for low-temperature CO oxidation over Pt/Ce@SSZ-13 catalyst with highly dispersed Pt-CeO_2 interfaces, Chem. Eng. J. 515 (2025) 163371.

[11] X. Fan, X. Qi, L. Li, High SO_2 resistance, ultra-low noble metal content, hydrophobic Pt/CeO_2 composites for CO oxidation, Colloid Surf. APhysicochem. Eng. Asp. 719 (2025) 137072.

[12] W. Chen, Y. Ma, F. Li, L. Pan, W. Gao, Q. Xiang, W. Shang, C. Song, P. Tao, H. Zhu, X. Pan, T. Deng, J. Wu, Strong electronic interaction of amorphous Fe_2O_3 nanosheets with Single-Atom Pt toward enhanced carbon monoxide oxidation, Adv. Funct. Mater. 29 (2019).

[13] Z. Li, S. Dai, L. Ma, Z. Qu, N. Yan, J. Li, Synergistic interaction and mechanistic evaluation of NO oxidation catalysis on Pt/Fe_2O_3 cubes, Chem. Eng. J. 413 (2021) 127447.

[14] P.J. Mafa, R. Patala, B.B. Mamba, D. Liu, J. Gui, A.T. Kuvarega, Plasmonic Ag_3PO_4/EG photoanode for visible light-driven photoelectrocatalytic degradation of diuretic drug, Chem. Eng. J. 393 (2020) 124804.

[15] D. Bajec, A. Kostyniuk, A. Pohar, B. Likozar, Micro-kinetics of non-oxidative methane coupling to ethylene over Pt/CeO_2 catalyst, Chem. Eng. J. 396 (2020) 125182.

[16] J. Ni, Z. Huang, W. Chen, Q. Zhou, X. Wu, H. Shen, H. Zhao, G. Jing, Unveiling platinum's electronic and dispersion impacts for enhanced benzene combustion: from nanoparticles to nanoclusters and single atoms, Chem. Eng. J. 482 (2024) 148819.

[17] X.-J. Lin, Y.-G. Sun, S.-J. Guo, S.-D. Zhang, Y. Liu, A.-M. Cao, Kinetically-controlled formation of Fe_2O_3 nanoshells and its potential in Lithium-Ion barreries, Chem. Eng. J. 433 (2022) 133188.

[18] L. Ma, X. Chen, J. Li, H. Chang, J.W. Schwank, Electronic metal-support interactions in Pt/FeO_x nanospheres for CO oxidation, Catal. Today 355 (2020) 539–546.

[19] A. Phakkhawan, P. Suksangrat, P. Srepusharawoot, S. Ruangchai, P. Klangtakai, S. Pimanpang, V. Amornkitbamrung, Reagent-and solvent-mediated Fe_2O_3 morphologies and electrochemical mechanism of Fe_2O_3 supercapacitors, J. Alloy. Compd. 919 (2022) 165702.

[20] R. Liu, H. Liu, B. Xu, Y. Wang, S. Li, Y. Wang, W. Xu, T. Zhu, The effect of Fe_2O_3 doping on a Pt/Co_3O_4 catalyst for CO oxidation: improvement of thermal stability and catalytic activity, Process Saf. Environ. Prot. 189 (2024) 1–10.

[21] R. Adhikary, D. Sarkar, M. Mukherjee, J. Datta, Remarkable performance of the unique Pd-Fe_2O_3 catalyst towards EOR and ORR: non-Pt and non-carbon electrode materials for low-temperature fuel cells, J. Mater. Chem. A. 9 (2021) 3052–3065.

[22] B.J. Cha, J.Y. Choi, Y. Ji, S. Zhao, S.Y. Kim, S.H. Kim, Y.D. Kim, Fe-oxide/Al_2O_3 for the enhanced activity of H_2S decomposition under realistic conditions: mechanistic studies by in-situ DRIFTS and XPS, Chem. Eng. J. 443 (2022) 136459.

[23] Y. Yu, J. Liu, Y. Yang, J. Ding, A. Zhang, Experimental and theoretical studies of cadmium adsorption over Fe_2O_3 sorbent in incineration flue gas, Chem. Eng. J. 425 (2021) 131647.

[24] E. Murphy, B. Sun, M. Ruescher, Y. Liu, W. Zang, S. Guo, Y.-H. Chen, U. Hejral, Y. Huang, A. Ly, I.V. Zenyuk, X. Pan, J. Timoshenko, B.R. Cuenya, E.D. Spoerke, P. Atanassov, Synergizing Fe_2O_3 nanoparticles on single atom Fe-N-C for nitrate reduction to ammonia at industrial current densities, Adv. Mater. 36 (2024) 2401133.

[25] X. Liu, X. Song, G. Jiang, L. Tao, Z. Jin, F. Li, Y. He, P. Dong, Pt Single-Atom collaborate with Pt Atom-Clusters by an In-Situ confined strategy for accelerating electrocatalytic hydrogen evolution, Chem. Eng. J. 481 (2024) 148430.

[26] M.-T. Zhu, K.-F. Zhang, W.-P. Du, A.-P. Jia, M.-F. Luo, J.-Q. Lu, Highly active and water tolerant Pt/MFe_2O_4 (M = Co and Ni) catalysts for low temperature CO oxidation, Appl. Catal. A. 619 (2021) 118142.

[27] X. Li, R. Dong, R. Zhang, Y. Zhang, P. Lu, X. Meng, P. Li, Performance improvement and the mechanisms of red mud oxygen carrier in chemical looping gasification using strontium doping strategy, Chem. Eng. J. 508 (2025) 160772.

[28] W. Cui, D. Xue, N. Tan, B. Zheng, M. Jia, W. Zhang, Pt supported on octahedral Fe_3O_4 microcrystals as a catalyst for removal of formaldehyde under ambient conditions, Chin. J. Catal. 39 (2018) 1534–1542.

[29] B. Wu, Y. Wu, J. Li, X. Zheng, L. Hu, B. Zhang, In-situ gas-modulating electron structure of Pt to boost NH_3-SCO reactions over Pt/Fe_3O_4, Sep. Purif. Technol. 359 (2025) 130514.

[30] T.G. Gambu, R.K. Abrahams, E. van Steen, Micro-Kinetic modelling of CO-TPD from Fe(100)-Incorporating lateral interactions, Catalysts 9 (2019) 310.

[31] S.M. Farhan, P. Wang, J. Yin, L. Cheng, Z. Chen, Exploring Pt-Cu synergistic effects on porous SiO_2 support with different Pt loadings for low-temperature oxidation of CO and C_3H_6, J. Environ. Chem. Eng. 12 (2024) 114677.

[32] X. Chen, C. Wu, Z. Guo, Synthesis of efficient Cu/$CoFe_2O_4$ catalysts for low temperature CO oxidation, Catal. Lett. 149 (2019) 399–409.

[33] J. Chen, S. Xiong, H. Liu, J. Shi, J. Mi, H. Liu, Z. Gong, L. Oliviero, F. Mauge, J. Li, Reverse oxygen spillover triggered by CO adsorption on Sn-doped Pt/TiO_2 for low-temperature CO oxidation, Nat. Commun. 14 (2023) 3477.

[34] P. Yang, C. Luo, W. Tan, Q. Liu, S. Zhang, S. Hong, F. Gao, L. Dong, Insights into the construction of robust Pt clusters with satisfactory stability on CeO_2 for the catalytic oxidation of CO, ACS Appl. Mater. Interfaces 16 (2024) 21782–21789.

[35] J. Li, S. Liu, L. Li, Y. Li, L. Wang, X. Chen, W. Yang, Introducing yttrium into Pt-based intermetallic compounds induce electron perturbation and anti-oxidation for enhancing oxygen reduction activity and durability, Chem. Eng. J. 501 (2024) 157849.

[36] J. Dong, Y. Zhang, D. Li, A. Adogwa, S. Huang, M. Yang, J. Yang, Q. Jin, Reaction-driven evolutions of Pt states over Pt-CeO_2 catalysts during CO oxidation, Appl. Catal. BEnviron. Energy 330 (2023) 122662.

[37] S.L. Le, C.R. O'Connor, T.-S. Kim, C. Reece, A metastable state facilitates low temperature CO oxidation over Pt nanoparticles, Angew. Chem. Int. Ed. 64 (2025) e202423880.